Journal of the Brazilian Society of Mechanical Sciences and Engineering (2023) 45:103
https://doi.org/10.1007/s40430-023-04031-1

TECHNICAL PAPER

Strain rate effect on CRALL under high-velocity impact by different projectiles

Bheekam Gaur[1] · Murlidhar Patel[1] · Shivdayal Patel[1]

Received: 17 September 2022 / Accepted: 10 January 2023 / Published online: 21 January 2023

Abstract
A fiber–metal laminate (FML) is a hybrid laminate that is mostly used for aircraft, automobiles, and defense industry applications. The carbon fiber-reinforced aluminum laminate (CRALL) is an advanced FML and has a very high specific strength. To investigate the effects of strain rate and projectiles' nose shape on the ballistic limit of the CRALL, a series of dynamic explicit analyses were performed at high-velocity impact (HVI) by using flat, hemispheric, and sharp-nosed projectiles at three distinct strain rates (1 s^{-1}, 100 s^{-1}, and 1000 s^{-1}). A progressive damage model based on damage initiation and damage propagation was developed for this numerical study and implemented in the ABAQUS software. At HVI, the damage modes and failure processes of the carbon fiber-reinforced polymer (CFRP) in the CRALL were investigated using Yens' criteria. The damage behavior of aluminum (Al) plates in the CRALL under HVI was determined by the Johnson–Cook (J-C) model. A cohesive surface based on bi-linear traction–separation law was utilized in between the Al plate and CFRP composite lamina to investigate the delamination in inter-laminar. The obtained results reveal that the CRALL has a high ballistic limit, either for high strain rates or for flat-nosed projectiles. The strain rate has significant influence on the CRALL ballistic limit velocities for the flat-nosed projectile as compared to other projectile configurations.

Keywords Ballistic · CRALL · FML · HVI · Projectile · Strain rate

1 Introduction

Fiber–metal laminates (FMLs) are combinations of monolithic metallic plates and composite laminates. The FMLs have abroad area of applications in various industries for technical as well as general purpose applications due to their good resistance to fatigue, impact, and fire resistance [1]. These industries may be the aerospace, automotive, and defense industries. In comparison to conventional plates and composite laminates, the use of FMLs reduces the weight of the structure while gaining excellent strength and corrosion resistance [2]. The FML materials currently used are Aramid fiber-reinforced aluminum laminates (ARALLs), glass-laminated aluminum-reinforced epoxy (GLARE), CRALLs, etc. [3].

Song et al. [4] experimentally and numerically investigated the energy absorption of CRALL through a drop-weight impact test. They showed that the object hit by 9.40 J exhibited matrix and fiber failures, whereas the object hit by 2.35 J exhibited no significant damage behavior appearing in CFRP layers but a shear fracture appearing on the Al layer. Naik et al. [5] observed that the glass fiber-reinforced plastic (GFRP) tensile strength increased by up to 88% at high strain rates as compared to the tensile strength at quasi-static loading. Rajkumar et al. [6] focused on the strain rate and lay-up configuration effects of the CRALL. They performed both tensile and flexural tests. They discovered that as the strain rate increased, the tensile strength increased but the flexural strength decreased. Naresh et al. [7] studied the effect of strain rates from 10 s^{-1} to 1000 s^{-1} to determine the sensitivity of the strain rate, tensile characteristics, and strain rate parameters. They also found that the tensile strength was proportional to the strain rate. Xia et al. [8] also found that CRALL tensile strength increases with respect to strain rate. Wen [9] studied the FMLs' impact behavior, which

Technical Editor: João Marciano Laredo dos Reis.

Shivdayal Patel
shivdayal@iiitdmj.ac.in

[1] Department of Mechanical Engineering, PDPM Indian Institute of Information Technology Design & Manufacturing, Jabalpur 482005, India

was perforated and pierced by oval as well as conical-nosed impactors at high velocities. He recorded that the truncated conical-nosed projectile provided the highest ballistic limit. Kpenyigba et al. [10] analyzed the impact behavior of an isotropic metal sheet under blunt, hemispheric, and conical-nosed projectiles of the same mass. As a result, the highest ballistic limit was observed for a hemispherical-nosed projectile, among others. Tirillo et al. [11] evaluated CFRP's ballistic limit at HVI and observed that hybridization of CFRP with basalt improved the ballistic limits. Xu et al. [12] experimentally reported that the CRALL has better penetration resistance against the HVI in comparison with the Al sheet and the CFRP laminate. Zhu et al. [13] numerically validated the Xu et al. [12] experimental results of ballistic limit and describe the damage behaviors of the CRALL under various projectile configurations impact. Many researchers [14, 15] implemented a continuum damage model via a VUMAT user-defined subroutine in ABAQUS to analyses composite laminate failures under impact loadings. Sierakowski [16] and Groves et al. [17] describe the influence of the strain rate on the mechanical behavior of the composite material. Yen [18] provided a numerical model to predict the strain rate impact on the composite material. Al-Hassaniand Kaddour [19]describe the strain rate effect of GFRP, CFRP and Kevlar fiber-reinforced polymer dynamic failure within the range of 5 s^{-1} to 400 s^{-1}. Hsiao and Daniel [20] discovered the composite stiffening follows a linear trend within the strain rate, which varies from 1 s^{-1} to 1800s^{-1}. Ma et al. [21] experimentally and Ma et al. [22] numerically represents the effect of strain rate on the ballistic limit of the GFRP composite. In these studies, they found the ballistic limit improved with an enhancement in the strain rate. To perform the numerical analysis, they used the material properties of strain rates ranging from 0.0001 to 0.01. Xiao et al. [23] numerically discovered the strain rate effect on the mild steel impact behavior subjected single particle impact. They have used the material properties of steel from 0.001 s^{-1} to 315 s^{-1}. They found the yield strength of the material increased with the rise in strain rate.

The experimental work on the FMLs subjected to HVI has been described in literature with various projectile shapes. The limited works on finite element simulation available for HVI with various nose-shaped projectiles with varying strain rates. However, in this numerical study, the effects of different-nosed (sharp, flat, and hemisphere) projectiles at strain rates of 1 s^{-1},100 s^{-1}, and 1000 s^{-1}have been analyzed on the CRALL's ballistic limit, residual velocity, damage behavior, and energy absorption under HVI. The progressive damage modeling of the CRALL materials has been developed using the damage initiation and damage evaluation model. The developed model has been implemented in the ABAQUS software to investigate the composite failures and validate the literature experimental results. An instantaneous elastic constant reduction approach has been utilized in this work to discover the material degradation during ballistic penetration, stress–strain characteristics, and type of failure.

2 Finite element modeling

2.1 Modeling of geometry

The geometry details of flat, hemispherical, and sharp-nosed projectiles of the same mass (30 g) are shown in Fig. 1. The finite element models of the CRALL with three different types of projectiles are shown in Fig. 2. All these configurations are taken from the literature [12, 13]. The CRALL has 2.4 mm thickness with 0.1 m in diameter. The CRALL and projectiles are discretized by using C3D8R and R3D4 elements, respectively. The CRALL has two 0.8 mm thick Al sheets and one 0.8 mm CFRP laminate [12]. The CFRP laminate has 8 plies of uniform thickness and ply orientations of $[0/90/0/90]_s$. The contact surfaces of each Al plate and each CFRP lamina are connected using cohesive modeling. The general contact modeling is used for connecting the CRALL and projectiles.

The circumferential edges of the CRALL's are fixed (arrest all degree of freedom) in all directions (*x*, *y*, *z*). This was done in simulations by employing a present velocity boundary condition. The friction coefficient of 0.3 is used between the CRALL and projectiles [13].

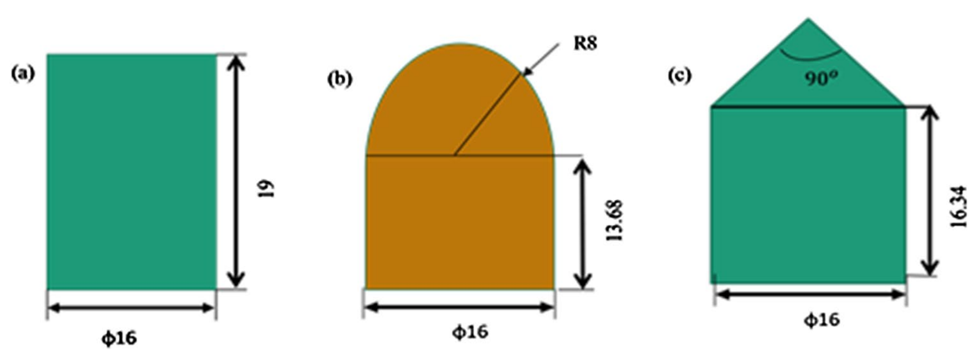

Fig. 1 Dimensions (in mm) of projectiles with **a** flat nose; **b** hemisphere nose; and **c** sharp nose

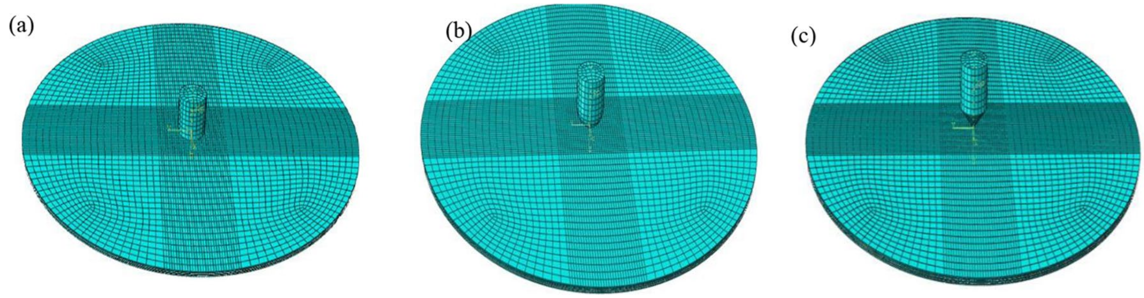

Fig.2 FE model of CRALLs with **a** flat nose; **b** hemispherical nose; and **c** sharp nose projectiles

2.2 Modeling of materials

2.2.1 J-C plasticity and damage model

The J–C model is generally applied to metals to predict the plastic damage during impact simulation problems like collisions and sudden weight drops from heights. The J–C model gives the coupled effect of strain, strain rate, and temperature [24]. The J-C plasticity model is expressed as:

$$\sigma = (A + B\varepsilon^n)\left[1 + C\ln\left(\frac{\dot{\varepsilon}}{\dot{\varepsilon_o}}\right)\right]\left[1 - \left(\frac{T - T_r}{T_m - T_r}\right)^m\right] \tag{1}$$

where; A, B, n, C, and m are material constants. T, T_m, and T_r are working, melting, and room temperature, respectively. $\dot{\varepsilon}$ is working strain rate and $\dot{\varepsilon_o}$ is reference strain rate. ε is equivalent plastic strain.

It not only depicts the build-up of the deformation process during failure but also the change in failure strain. The stress state, strain rate, and temperature are used to calculate the plastic failure strain ε_f.

$$\varepsilon_f = \left[D_1 + D_2\exp(D_3\sigma^*)\right]\left[1 + D_4\ln\left(\frac{\dot{\varepsilon}}{\dot{\varepsilon}_o}\right)\right]\left[1 + D_5\left(\frac{T - T_r}{T_m - T_r}\right)\right] \tag{2}$$

where D_i ($i = 1, 2, \ldots, 5$) are known as failure damage parameters. The curve fitting of the calibrated relationship between failure strain and stress tri-axiality at room temperature can be used to find the values D_1, D_2, D_3, and D_4. For D_5 least square method can be used. An accumulation of damage parameter is determined by Eq. (3)

$$D = \Sigma\frac{\Delta\varepsilon_f}{\varepsilon_f} \tag{3}$$

For an integration cycle, the equivalent plastic strain increment is denoted here by $\Delta\varepsilon_f$.

The properties with all these J-C parameters of Al plate are represented in Table 1.

Table 1 Materials properties used for Al 2024-T3 [13]

E (GPa)	μ	ρ (kg/m^3)	A (MPa)	B (MPa)
72.2	0.35	2750	369	684
T_r(K)	T_m(K)	n	M	C
269	775	0.73	1.7	0.0083
D_1	D_2	D_5	D_3	D_4
0.112	0.123	0	1.5	0.007

2.2.2 Constitutive relation of CFRP

In this analysis, to find the modulus at a high strain rate, Karim's [25] rules of mixture for a unidirectional composite are used, as given by:

$$\begin{aligned} E_{11}(t) &= E_{f1}V_f + V_m\left[E_m + Qe^{-Mt} + Re^{-Nt}\right] \\ E_{22}(t) &= \frac{E_{f1}V_f}{E_{f2}\dot{V}_m + E_{f1}\dot{V}_f} + Qe^{-Mt} + Re^{-Nt} \\ G_{12}(t) &= \frac{G_{f12}G_m}{G_{f12}\dot{V}_m + G_m\dot{V}_f} + Q_{12}e^{-Mt} + R_{12}e^{-Nt} \\ G_{23}(t) &= \frac{G_{f23}G_m}{G_{f23}\dot{V}_m + G_m\dot{V}_f} + Q_{23}e^{-Mt} + R_{23}e^{-Nt} \end{aligned} \tag{4}$$

The details about these parameters are provided in the literature [25]. The above relationships are used to obtain the values of all elastic moduli at constant strain rate. The values of these parameters for CFRP are shown in Table 2, where E_1 and E_2 are Maxwell elements.

2.2.3 Damage model of CFRP

Damage initiation criteria developed by Yen [18] have been employed by VUMAT in ABAQUS to predict the types of failure modes for unidirectional composites. These criteria are an extension of Hashins' composite failure model. Failure criteria are given for fiber and matrix damages by Yen [18] are represented in Eqs. (5)-(9):

Fiber damage:

Uniaxial tension and transverse shear;

Table 2 CFRP engineering constants [13]

Properties	ρ (kg/m^3)	E_1 (GPa)	E_2 (GPa)	E_m (GPa)	G_m (GPa)	υ_{23}	$\upsilon_{12} = \upsilon_{13}$
Value	1570	0.971	0.104	2.31	0.857	0.38	0.25
Properties	E_{f1} (GPa)	E_{f2} (GPa)	$G_{f12}=G_{f13}$(GPa)	G_{f23}(GPa)	θ_{e1} (ms)	θ_{g1} (ms)	$\theta_{e2}=\theta_{g2}$ (ms)
Value	230	15	2.35	24	0.041	0.077	121,000

$$f_1 - r_1^2 = \left(\frac{E_{11}\langle\varepsilon_{11}\rangle}{S_{XT}}\right)^2 + \frac{G_{12}^2\varepsilon_{12}^2 + G_{13}^2\varepsilon_{13}^2}{S_{FS}^2} - r_1^2 = \begin{cases} < 1 \text{ no failure} \\ \geq 1 \text{ failure} \end{cases} \tag{5}$$

Uniaxial compression;

$$f_2 - r_2^2 = \left(\frac{E_{22}\langle\varepsilon_{11}'\rangle}{S_{XC}}\right)^2 - r_2^2 = \begin{cases} < 1 \text{ no failure} \\ \geq 1 \text{ failure} \end{cases} \tag{6}$$

Transverse compression;

$$f_3 - r_3^2 = \left(\frac{E_{22}\langle-\varepsilon_{22}\rangle}{S_{FC}}\right)^2 + \left(\frac{E_{33}\langle-\varepsilon_{33}\rangle}{S_{FC}}\right)^2 - r_3^2 = \begin{cases} < 1 \text{ no failure} \\ \geq 1 \text{ failure} \end{cases} \tag{7}$$

Matrix damage:
Perpendicular direction;

$$f_4 - r_4^2 = \left\{\left(\frac{E_{22}\langle\varepsilon_{22}\rangle}{S_{Yut}}\right)^2 + \left[\frac{G_{23}\varepsilon_{23}}{S_{YZ0} + S_{YSR}}\right]^2 + \left[\frac{G_{12}\varepsilon_{12}}{S_{XY0} + S_{YSR}}\right]^2\right\} - r_4^2 = \begin{cases} < 1 \text{ no failure} \\ \geq 1 \text{ failure} \end{cases} \tag{8}$$

Parallel direction (delamination);

$$f_5 - r_5^2 = \left\{\left(\frac{E_{33}\langle\varepsilon_{33}\rangle}{S_{Zut}}\right)^2 + \left[\frac{G_{23}\varepsilon_{23}}{S_{YZ0} + S_{YSR}}\right]^2 + \left[\frac{G_{13}\varepsilon_{13}}{S_{XZ0} + S_{ZSR}}\right]^2\right\} - r_5^2 = \begin{cases} < 1 \text{ no failure} \\ \geq 1 \text{ failure} \end{cases} \tag{9}$$

Here;

$$\varepsilon_{11}' = \max\left\{-\varepsilon_{11} - \langle\varepsilon_{22}\rangle\frac{E_{22}}{E_{11}}, -\varepsilon_{11} - \langle\varepsilon_{33}\rangle\frac{E_{33}}{E_{11}}\right\}$$

Here; $\varepsilon_{11}, \varepsilon_{22}, \varepsilon_{33}, \varepsilon_{12}, \varepsilon_{23}, and \varepsilon_{13}$ are ply-level engineering strains. E_{11}, E_{22}, E_{33}, G_{12}, G_{23}, and G_{13} are associated elastic moduli. Macaulay brackets represented here by⟨⟩.Tensile strength, compressive strength, fiber layer shear strength, and crush failure strength are represented by S_{XT}, S_{XC}, S_{FS}, and S_{FC}, respectively. For the initial damage-free material, damage thresholds r_i (i=1,2,3,…) are set to 1.

For damage evolution, to quantify six damage variables $\overline{\omega}_i$ with i = 1, 2,….6 are assumed and corresponding compliance matrix has been developed as:

$$[S] = \begin{bmatrix} \frac{1}{(1-\overline{\omega}_1)E_{11}} & \frac{-\upsilon_{21}}{E_{22}} & \frac{-\upsilon_{31}}{E_{33}} & 0 & 0 & 0 \\ \frac{-\upsilon_{12}}{E_{11}} & \frac{1}{(1-\overline{\omega}_2)E_{22}} & \frac{-\upsilon_{32}}{E_{33}} & 0 & 0 & 0 \\ \frac{-\upsilon_{13}}{E_{11}} & \frac{-\upsilon_{23}}{E_{22}} & \frac{1}{(1-\overline{\omega}_3)E_{33}} & 0 & 0 & 0 \\ 0 & 0 & 0 & \frac{1}{(1-\overline{\omega}_4)G_{12}} & 0 & 0 \\ 0 & 0 & 0 & 0 & \frac{1}{(1-\overline{\omega}_5)G_{23}} & 0 \\ 0 & 0 & 0 & 0 & 0 & \frac{1}{(1-\overline{\omega}_6)G_{13}} \end{bmatrix} \tag{10}$$

Stiffness matrix is the inverse of compliance matrix and is obtained by inverting them

$$[C] = [S]^{-1} \tag{11}$$

The growth rate is defined by damage evolution law as given below

$$\overline{\omega}_i = \sum_j \dot{\psi}_j q_{ji} \tag{12}$$

where; $\dot{\psi}_j(i = 1, 2 \ldots)$ is the scalar function, 'j' is growth rate, and q_{ji} couples both the damage variable and scalar function.

2.2.4 Formulations for strain rate dependence

The significant effects of strain rate on the composite laminate properties during the HVI are observed. When this influence is considered, the strength and stiffness of unidirectional composites alter. The unidirectional CFRP composite strengths are modified with respect to changes in strain rate as per the following equation [18]:

$$\{S_{RT}\} = \{S_0\}\left(1 + c\ln\frac{\{\dot{\varepsilon}\}}{\dot{\varepsilon}_0}\right) \tag{13}$$

Table 3 Properties of unidirectional CFRP at different strain rates

Properties of CRALLs		$1\ s^{-1}$	$100\ s^{-1}$	$1000\ s^{-1}$
Stiffness (GPa)	E_{11}	139.32	203.407	235.450
	E_{22}	3.1	4.526	5.239
	E_{33}	3.1	4.526	5.239
	G_{12}	0.95	1.387	1.605
	G_{13}	0.95	1.387	1.605
	G_{23}	1.3	1.898	2.197
Strength (MPa)	X_T	2050	2994	3464
	X_C	1050	1534	1774
	Y_T	71	104	120
	Y_C	132	193	223
	S_L	75	110	126
	S_T	34	54	57
Fracture energy (N/m)	G_{1T}	48,400	19,910.43	23,038
	G_{1C}	60,300	10,198.04	11,800
	G_{2T}	4500	68,953.85	79,793
	G_{2C}	8500	128,198.7	148,348

$$\text{Here; } \{S_{RT}\} = \begin{Bmatrix} X_T \\ X_C \\ Y_T \\ Y_C \\ S_L \\ S_T \end{Bmatrix}_{RT} \text{ and} \{S_O\} = \begin{Bmatrix} X_T \\ X_C \\ Y_T \\ Y_C \\ S_L \\ S_T \end{Bmatrix}_O \text{ where}$$

$c = 0.1$ is the strain rate constant, $\{S_0\}$ and $\{S_{RT}\}$ are the strengths at reference strain rate ($\dot{\varepsilon}_0$) and current strain rate ($\dot{\varepsilon}$), respectively.

The strain rate impacts on elastic moduli are extracted in the same way as:

$$\{E_{RT}\} = \{E_0\}\left(1 + c\ln\frac{\{\dot{\varepsilon}\}}{\dot{\varepsilon}_0}\right) \tag{14}$$

$$\text{Here; } \{E_{RT}\} = \begin{Bmatrix} E_{11} \\ E_{22} \\ E_{33} \\ G_{12} \\ G_{13} \\ G_{23} \end{Bmatrix}_{RT} \text{ and} \{E_O\} = \begin{Bmatrix} E_{11} \\ E_{22} \\ E_{33} \\ G_{12} \\ G_{13} \\ G_{23} \end{Bmatrix}_O$$

Here, $\{E_0\}$ and $\{E_{RT}\}$ are the elastic moduli at reference strain rate ($\dot{\varepsilon}_0$) and current strain rate ($\dot{\varepsilon}$), respectively. During HVI, the composite laminates show a noticeable strain rate effect. Considering the $1\ s^{-1}$,$100\ s^{-1}$, and $1000\ s^{-1}$ strain rates' effect on the CFRP strengths, the rate-dependent parameters of strength are calculated by using Eqs. 13 and 14. By increasing the strain rate, increases in the strength and stiffness properties of composite (CFRP) were obtained. All calculated properties are given in tabular form in Table 3

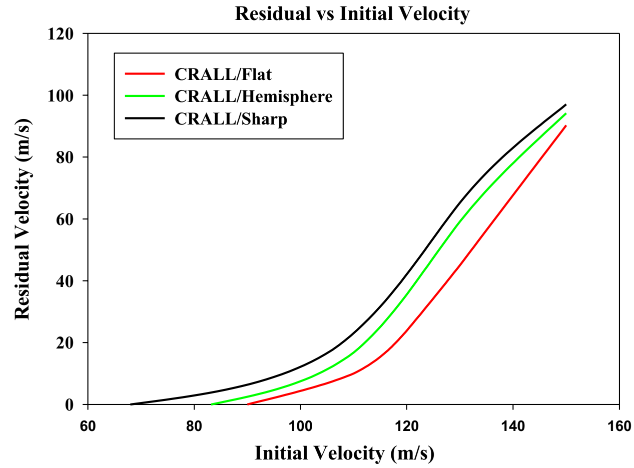

Fig. 3 Residual velocity versus initial velocity curves for various projectiles

and used to find residual velocity, ballistic velocity, stresses, and energy absorption. The fracture energies at different strain rates are also listed in Table 3.

2.2.5 Damage mode of interface

For interfaces, delamination is the crucial failure mechanism of FMLs when they are subjected to HVI. An energy-based Benzeggagh–Kenane (B–K) power law was employed [26] to analyses the delamination behavior.

The interface is very thin, with only two shear tractions and normal traction acting. The delamination is unavoidable under mixed-mode conditions. Nominal stress criterion for mixed-mode conditions is given by:

$$\left(\frac{\sigma_n}{N}\right)^2 + \left(\frac{\sigma_s}{S}\right)^2 + \left(\frac{\sigma_t}{T}\right)^2 = 1 \tag{15}$$

Here, S, T, and N are defined as maximum stress values for the corresponding two shear and one normal direction, respectively, while σ_n, σ_s, and σ_t denote the traction stress in those directions. The cohesive properties are taken from literature [26, 27].

2.3 Validation of numerical model

The Yens' criteria and J-C damage modeled are employed for CFRP composite laminate and metallic Al plates, respectively, to validate the present numerical results with literature [12] experimental results for ballistic limit of CRALL under the velocity range from 60 to 150 m/s. A ballistic velocity is the highest impactor's starting velocity at which it fails to perforate the target plate. The ballistic velocities as predicted by the present numerical models of

Table 4 Experimental [12] and present numerical results comparisons for ballistic limit of CRALLs

Model	Experiment [12] (m/s) (*p*)	Prediction [13] (m/s) (*q*)	Present simulation (m/s) (*r*)	% Error between (*p*) and (*r*)
CRALL/F	85.2	108.7	90.02	5.8
CRALL/H	80.9	84.4	83.2	2.8
CRALL/S	70.5	67.8	68	3.5

CRALL for three distinct projectile combinations named CRALL/Flat (CRALL/F), CRALL/Hemispherical (CRALL/H), and CRALL/Sharp (CRALL/S) are shown in Fig. 3. The CRALL/S and CRALL/F versions have somewhat more nonlinear behavior than the CRALL/H. Table 4 shows the CRALLS' ballistic limit comparisons of the current study with both the experimental and numerical results of Xu et al. [12] and Zhu et al. [13], respectively, at 1 s^{-1} strain rate for distinct nose projectile impacts. Small percentage errors are seen between the obtained results and the literature [12] experimental results. By applying fine meshing only in the impact zone (as shown in Fig. 2), we were able to save computational time while maintaining the accuracy of the results. After validation at a strain rate of 1 s^{-1}, FE modeled CRALL with various nose-shaped projectiles are utilized to explore the ballistic limit in greater depth throughout the ballistic penetration process at higher strain rates.

The numerically obtained failure behavior of the various CRALL configurations at the reference strain rate (1 s^{-1}) is compared with the experimentally [12] deformed CRALL configurations. The modes of failure of the top Al plate, followed by the top CFRP laminate and the bottom Al plate, are compared for the present numerical and literature experimental [12] case. These comparisons are illustrated in Fig. 4. This figure clearly shows the numerically fractured Al plates and CFRP laminate patterns are matched with the experimental fracture modes for all configurations. For the case of CRALL/F at velocity of V_{110}, the top and bottom Al plates are subjected to shear damage and both tensile and shear damage, respectively. Similarly, for the CRALL/H configuration at velocity of V_{107}, only a ductile fracture hole is seen in the top Al plate. CFRP and the bottom Al plate are subjected to two orthogonal cracks and two orthogonal fractured holes, respectively. The CRALL/S fracture behaviors are the same as the CRALL/H configuration, but due to the smaller contact area of the sharp-nosed projectile as compared to the hemisphere-nosed projectile, a small hole is created on the top al plate.

3 Results and discussion

Dynamic explicit analysis on the CRALL is performed using the different projectile's nose shapes with strain rate effect consideration. The ballistic limits and residual velocities of the CRALL are determined using progressive damage modeling. The Yen criteria and J–C model are used for damage behavior prediction of CFRP and Al respectively. The obtained results for the ballistic limit, residual velocity, damage failure behavior, and energy absorption are discussed in the below sections.

3.1 Effect of strain rate on the ballistic limit of CRALL

The projectile's nose shape at various strain rates influences the ballistic limit as well as the residual velocity of the CRALL. To evaluate the ballistic velocity of the CRALL/F configuration, ten successive hits for each strain rate (1 s^{-1}, 100 s^{-1}, and 1000 s^{-1}) were applied to the CRALL by a flat-nosed projectile. The projectile starting velocities ranging from 80 to 180 m/s were used to perform this study. Figure 5a illustrates a flat-nosed projectile's residual velocities (terminal velocity) variation with respect to flat-nosed projectile starting velocity at 1 s^{-1}, 100 s^{-1}, and 1000 s^{-1} strain rates. The starting velocity varies from 80 m/s to 180 m/s, with the highest ballistic limit of 122 m/s obtained at 1000 s^{-1} strain rate. The ballistic limits of the CRALL/F configuration at 1 s^{-1} and 100 s^{-1} are obtained at 90.02 m/s and 120 m/s, respectively. At a projectile starting velocity of 130 m/s (V_{130}), the residual velocities are 45 m/s, 34.02 m/s, and 30.52 m/s for 1 s^{-1}, 100 s^{-1}, and 1000 s^{-1} strain rates, respectively. The residual velocities at V_{150} are 90.26 m/s, 85.43 m/s, and 82.97 m/s for 1 s^{-1}, 100 s^{-1}, and 1000 s^{-1}, respectively. As a result, at 1000 s^{-1} strain rate, the residual velocity is the smallest, followed by 100s^{-1} and 1 s^{-1}strain rates. This increase in ballistic limit and decrease in residual velocity with an increase in strain rate is due to the enhancement in the stiffness of both Al plates and CFRP laminate [16, 17, 28, 29]. In the case of a higher strain rate, the CRALL strength increases due to the restriction of dislocation movements. However, the CRALL/F configuration gives the highest ballistic limit and the smallest residual velocity for 1000 s^{-1} strain rate.

Similarly, a series of nine successive impacts applied by a hemisphere-nosed projectile of diverse strain rates (1 s^{-1},100 s^{-1}, and 1000 s^{-1}) on the CRALL at various starting velocities. The starting velocities of hemisphere-nosed projectile ranging from 60 to 150 m/s to determine the ballistic limit and residual velocities behavior of the

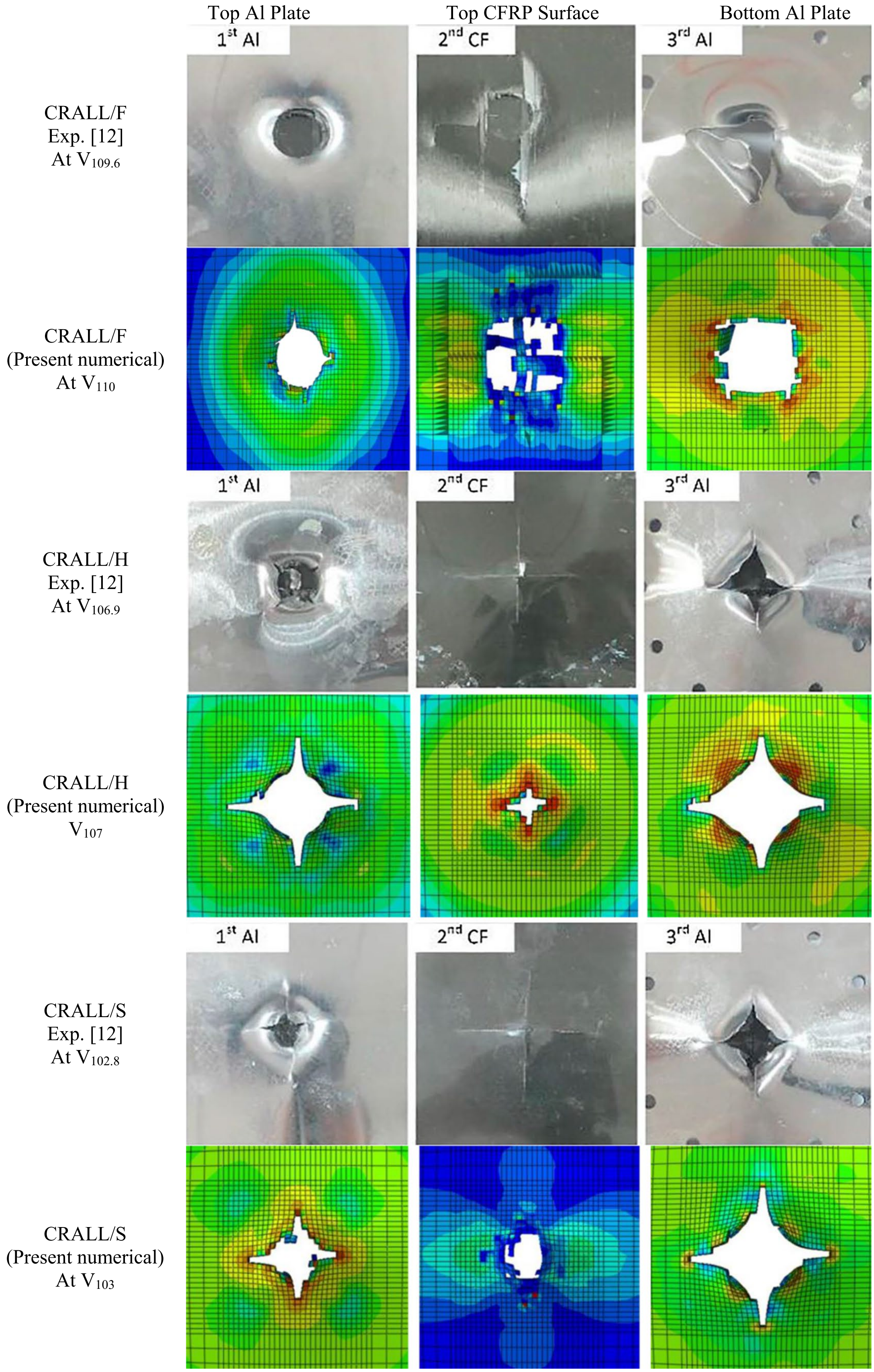

Fig. 4 Modes of CRALLs fracture under HVI by various projectiles

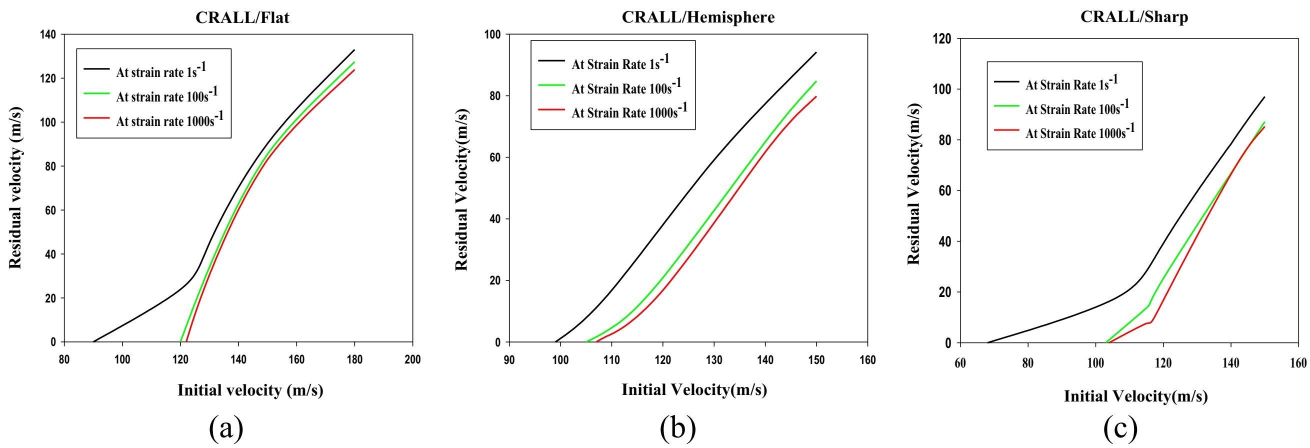

Fig.5 Residual-initial velocity curves for different projectiles at different strain rates

CRALL/H configuration as illustrated in Fig. 2b. Figure 5b represents the variation of residual velocity with respect to hemisphere-nosed projectile starting velocity at various strain rates. At 1 s^{-1}, 100 s^{-1}, and 1000 s^{-1} strain rates, the ballistic limits of the CRALL/H configuration are obtained as 83.2 m/s, 105 m/s, and 107 m/s, respectively. The strain rate influences the residual velocities of the projectile. The projectile residual velocity is also a function of the starting projectile velocity. From Fig. 5b, it is observed that for 1 s^{-1}, 100 s^{-1}, and 1000 s^{-1} strain rates, the hemisphere-nosed projectile residual velocities at V_{130} are 58.66 m/s, 42.93 m/s, and 39.25 m/s, respectively. Similarly, at V_{150} these are recorded as 94.15 m/s, 84.73 m/s, and 83.81 m/s, respectively, for 1 s^{-1}, 100 s^{-1}, and 1000 s^{-1} strain rates. This could be because the CRALL stiffens at high strain rates as the yield strengths of both Al and CFRP increase. The stiffer CRALL restricts the projectile's ability to pass through it under high strain rate conditions. However, the residual velocity varies in inverse proportion to the strain rate [22].

To determine the ballistic velocity of the CRALL/S configuration depicted in Fig. 2c, eight successive impacts on the CRALL were applied for each strain rate by a sharp-nosed projectile. The sharp-nosed projectile's starting velocity varies between 60 and 150 m/s to identify the ballistic limit of the CRALL/S configuration. Figure 5c represents the relation between residual and starting velocities of the CRALL/S at different strain rates. The ballistic limits recorded at 1 s^{-1}, 100 s^{-1}, and 1000 s^{-1} strain rates for the CRALL/S configuration are 68 m/s, 103 m/s, and 104 m/s, respectively. The ballistic limit obtained at 1 s^{-1} is the smallest, followed by 100s^{-1} and 1000 s^{-1}. At V_{130}, the residual velocities of 59.14 m/s, 45.91 m/s, and 41.58 m/s are recorded for 1 s^{-1}, 100 s^{-1}, and 1000 s^{-1} strain rates, respectively. For a starting velocity of 150 m/s, the highest residual velocity of 97.04 m/s obtained at 1 s^{-1} strain rate, followed by 87.13 m/s at 100 s^{-1}, and 85.24 m/s at 1000 s^{-1}, as seen in Fig. 5c. Fig. 5 clearly indicates that the residual velocity of a projectile is a function of both the starting velocity of the projectile and the strain rate. Strain rate has a significant influence on residual velocity and ballistic limit, as revealed in Fig. 5. A sharp-nosed projectile has the highest residual velocity for a fixed projectile starting velocity due to its small initial contact area with the CRALL at all strain rates, followed by hemisphere and flat-nosed projectiles. The higher contact area of the projectile with the CRALL increases the friction between them. However, the flat-nosed projectile's residual velocity is the smallest among the other projectile configurations [13]. The increase in the strain rate strengthens the CRALL, which causes the perforation capacity of the projectile to reduce. Therefore, at high strain rate, residual velocity is minimum for all projectile shape [19, 30].

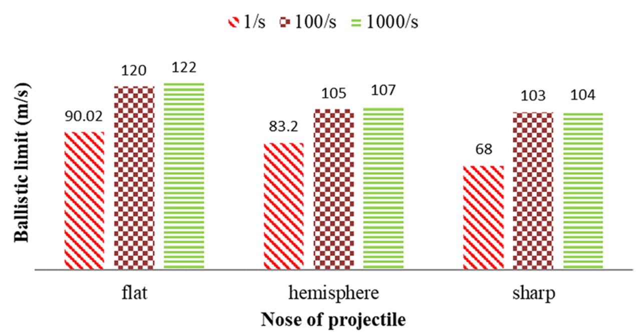

Fig. 6 CRALL ballistic limit at different strain rates

The comparisons of the ballistic limit velocity are demonstrated in Fig. 6 for three separate projectiles at three different strain rates. The results plotted in Fig. 6 show that the ballistic velocity of the CRALL increases for all three projectile models with raising in strain rate. Sharp and flat

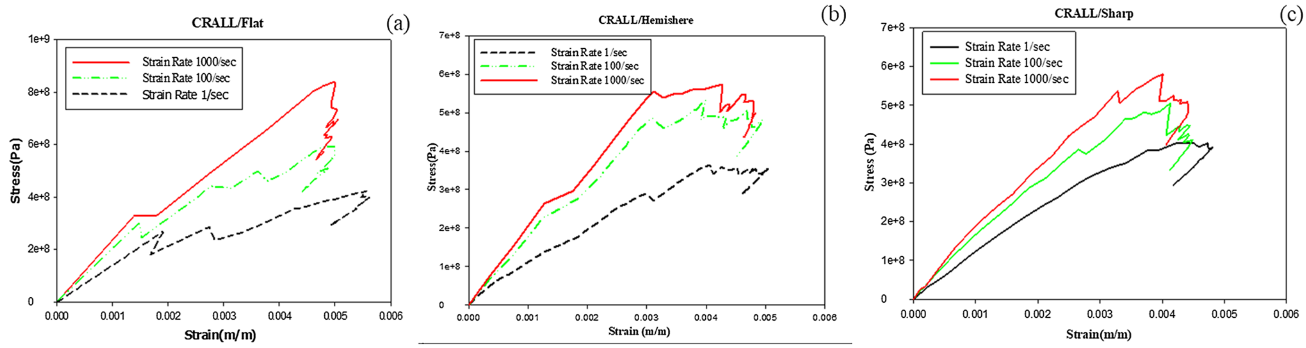

Fig. 7 Stress–strain curves for CRALL at different strain rates and projectiles

projectiles demonstrated that the CRALLs ballistic velocities are lowest and maximum, respectively. This could be due to the nose contact area of the flat projectile is higher followed by hemisphere and sharp-nosed projectile. The larger contact area of the projectile has less perforation capacity in comparison with the smaller contact area of the nosed projectile. However, the CRALL/H configuration shows an intermediate nature as compared to the CRALL/F and CRALL/S configurations. The CRALL ballistic limit velocity for hemisphere projectile changes relatively little (28.6%) with regard to the varied strain rates (1 to 1000 s^{-1}) followed by flat (35.52%) and sharp (52.94%) and identified the low residual velocity at high strain rate. Due to an increase in the strength of both the Al and CFRP of the CRALL for increased strain rate, the ballistic limit of the CRALL improved for all projectile configurations. This mechanism of strengthening the CRALL with a high strain rate is discussed in Sect. 3.2.

3.2 Strain rates effects on stress–strain characteristics

Stress–strain behavior of both the Al plate and the CFRP laminate is influenced by the rate of strain applied. The effect of strain rate on the stress–strain characteristics of various CRALL configurations is illustrated in Fig. 7. At low strain rates, ductile material (Al plates) has time to stretch before breaking. The maximum load is therefore limited. However, a material has less time to deform at a high strain rate, which results in a larger measured load. Dislocation glide or twinning is the two types of atomic mobility that determine the yield phenomenon for ductile materials. The dislocation glide is disrupted by a high strain rate, which prevents twinning. This method has a higher yield point since it takes more energy to shift atoms. As the strain rate rises, the overall elongation decreases during the projectile's impact [23, 29–32]. Similarly, in the case of CFRP composite laminate, the material stiffens as the strain rate rises (with a decrease in matrix ductility). This stiffening behavior has a substantial impact on the ballistic limit. There are different proposed explanations for this phenomenon. The viscoelastic properties of the polymeric matrix itself make up the first, while the time-dependent nature of accumulated damage makes up the second [20]. When damage happens more gradually and at slower rates, a clearly defined nonlinear zone appears close to the stress–strain curve's terminus. This behavior can be clearly seen in Fig. 7 for all CRALL configurations. Since the loading period is brief enough for material failure to occur before the commencement of fiber initiation failure, the Young's modulus of elasticity rises with strain rate [33]. This implies that when the strain rate rises, the failure modes shift. Materials that are lightly cross-linked will experience significant elastic deformation before breaking, whereas uncross-linked polymers will exhibit viscoelastic behavior. The behavior before breaking will depend on the crosslink and entanglement densities [18, 19]. However, for high strain rates, the CRALL has high yield strength for all impact cases with various nose-shaped projectiles. During the impact on the CRALL, plug formed on the CRALL and is more at the high strain at the same time instant. Figure 7a depicts the stress–strain relation at various strain rates for the CRALL/F configuration. From Fig. 7a, it is noted that the rate of strain is increased from 1 to 100 s^{-1}, the modulus of elasticity rises by 45.99%, resulting in a 12.40% increase in yield strength, and the maximum strength rises by 41.58%. Similarly, as the strain rate is raised from 100 to 1000 s^{-1}, the modulus of elasticity increases by 15.75%, resulting in enhanced yield strength and maximum strength of 9.97% and 40.25%, respectively.

The stress–strain curves for the CRALL/H are shown in Fig. 7b. For the CRALL/H, the modulus of elasticity increases by 45.99% when the strain rate is raised from 1 to 100 s^{-1}, resulting in a 67.75% increase in yield strength and a 46.48% increase in maximum strength. The modulus of elasticity rises by 15.75% as the strain rate is increased from 100 to 1000 s^{-1}, resulting in increased yield strength and maximum strength of 13.88% and 7.58%, respectively. From Fig. 7c, it revealed that for the CRALL/S, when the rate of

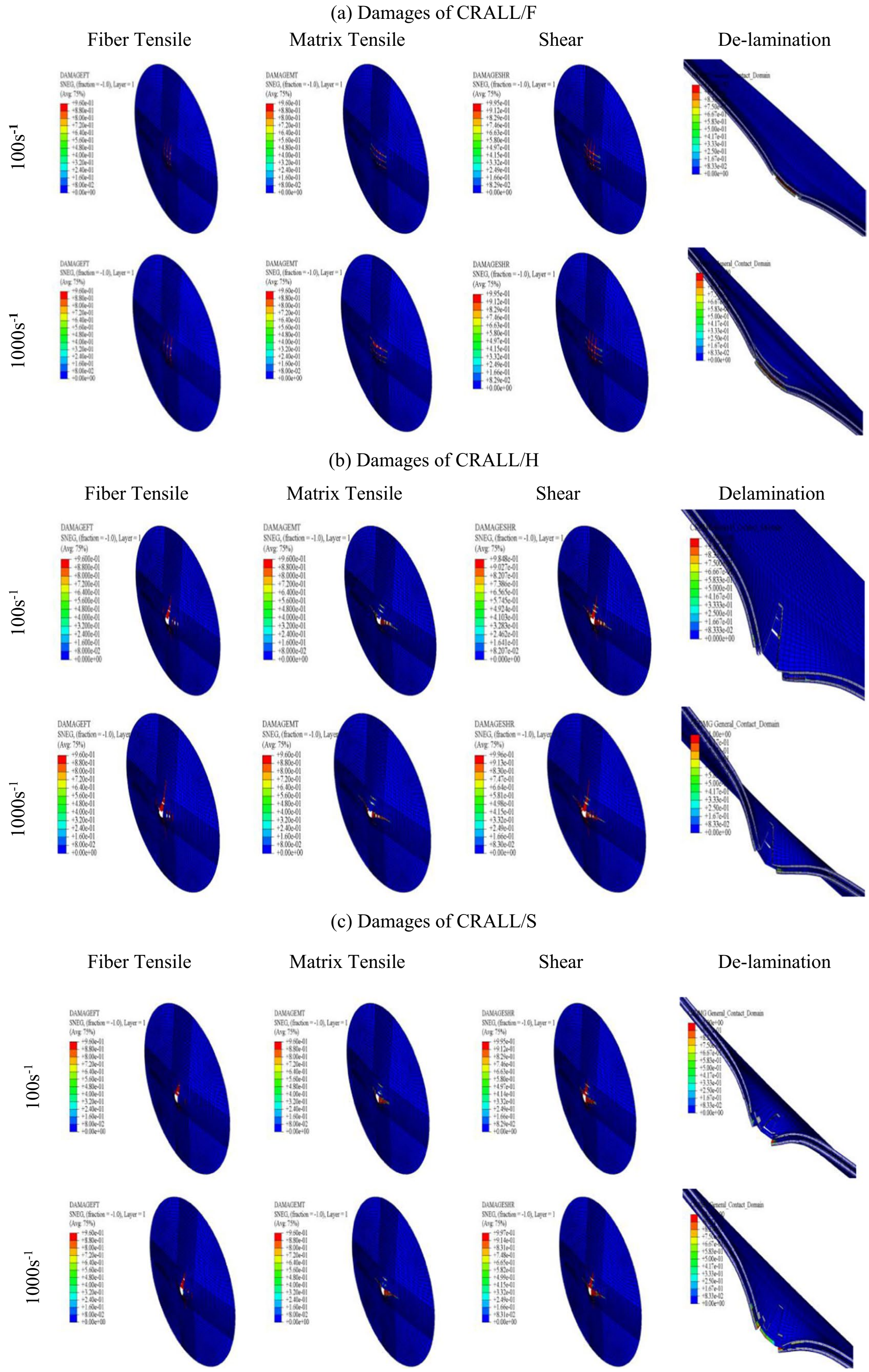

Fig. 8 Damages at 100 s^{-1} and 1000 s^{-1} strain rates in CRALLs

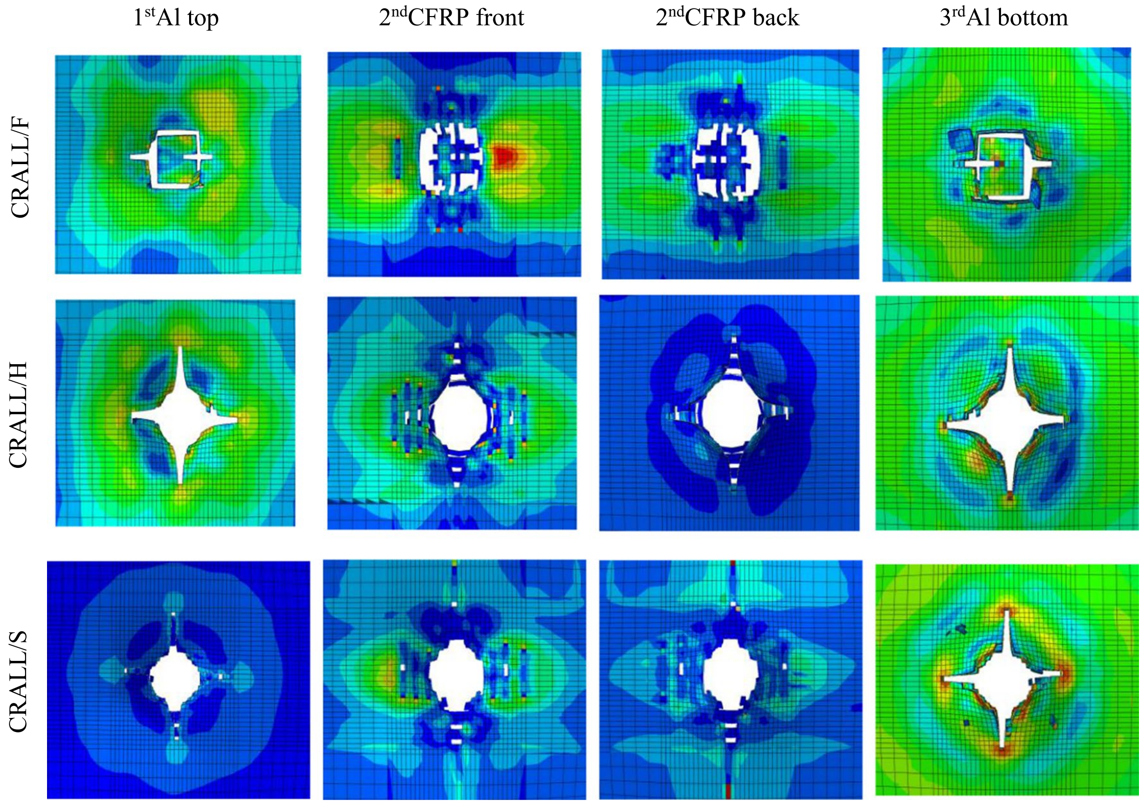

Fig. 9 Damaged area of CRALL at high strain rates

strain is increased from 1 to 100 s^{-1}, the modulus of elasticity rises by 45.99%, resulting in a 0.51% increase in yield strength and a 26.46% increase in maximum strength. When the rate of strain is raised from 100 to 1000 s^{-1}, the modulus of elasticity increases by 15.75%, resulting in enhanced yield strength and maximum strength of 36.60% and 14.75%, respectively. These improvements in the CRALLs' strength are due to a rise in the strain rate [22, 25, 29].

3.3 CRALL failure analysis

The tensile, shear, and delamination failures operated on the all CRALL models in both 100 s^{-1} and 1000 s^{-1}strain rates shown in Fig. 8. The delamination criterion worked appropriately in both strain rate models without reducing the strain rate impact. For the CRALL/F model, increased strain rates have a little influence on fiber and matrix tensile failures in CFRP. The enhanced strain rate (100–1000 s^{-1}) increases the shear effect. For a high strain rate, the delamination in CFRP laminate of the CRALL is greater than the low strain rate delamination. The laminate shows the tensile cracks caused by flat-nosed projectile impacts at high strain rates. Fiber tensile, matrix tensile, and shear failure occurred in the CRALL/H model at both strain rates, as shown in Fig. 8b. Increased strain rate had little influence on fiber and matrix tensile in the CFRP composite laminate. However, the enhanced strain rate increased the shear effect on the CRALL's CFRP laminate. A diamond-shaped bulge formed due to impact by a hemisphere-nosed projectile. This bulge size is higher for 1000 s^{-1} strain rate as compared to 100 s^{-1}. Figure 8c depicts the tensile fiber and matrix failure as well as shear and delamination in the CFRP laminate during impact by a sharp-nosed projectile. The CRALL/S configuration also shows a similar type of failure as seen for the CRALL/H configuration. In the CRALL/S configuration, the damage area is smaller than the damage area of the CRALL/H configuration. This could be due to the smaller contact area of a sharp-nosed projectile. For all CRALL configurations, the damage in the CFRP is a little bit higher for high strain rates. This could be due to the fact that the crack formed during the projectile's impact propagates faster for the high strain rate. Figure 8 represents the shear damage is the major failure of the CFRP laminate followed by the matrix tensile failure and fiber tensile failure, respectively, in the entire CRALL configuration.

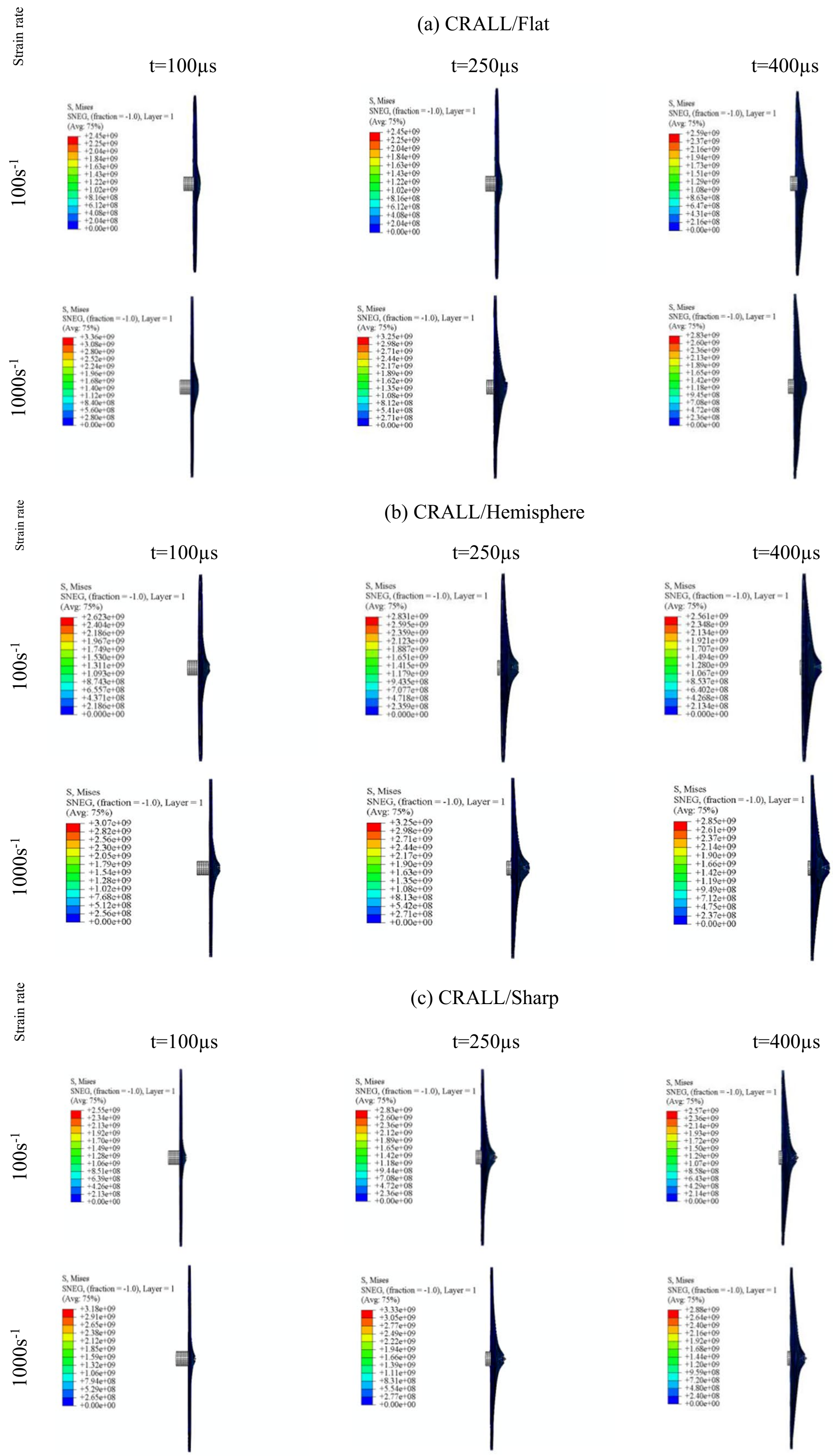

Fig. 10 Ballistic penetration process of CRALL

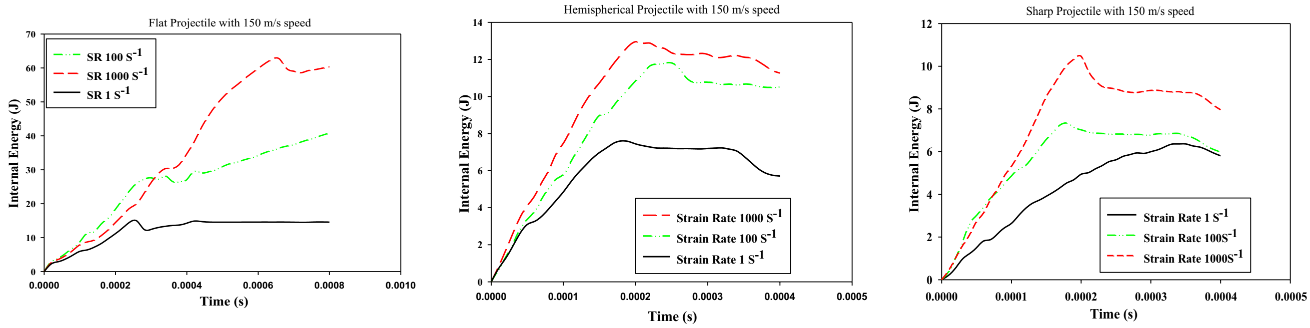

(a) (b) (c)

Fig. 11 Energy absorption for various configurations

3.4 Analysis of ballistic penetration process

Figure 10 shows the various nosed projectiles' ballistic penetration process (at 100 s^{-1} and 1000 s^{-1} strain rate) in the CRALL at different times. As shown in Fig. 10a for flat-nosed projectile, penetration is the largest at $t = 100$ µs because its impacted face contacts area is very large as compared to sharp and hemisphere nose.

The plasticity of the composite plate is lower as compared to aluminum sheets. As we increase strain rate, deformation will be increased at the same time instant. Therefore, at $t = 250$ µs it can be easily see, a plug column is started. This plug formation is a plugging part of CRALL but is more at the high strain at the same time instant. Due to high shearing in the case of a flat-nosed projectile, no plug ejection is seen in Fig. 9. In the composite layers, tensile shear failure and delamination occur between the Al layer and composite layer. Shear failure dominated due to the edge of the flat nose. At $t = 400$ µs afterward, since the projectile no longer deformed the CRALL plate, and perforated area no longer increased after increasing the time (> 400 µs). The depth of penetration of a projectile increases as we increase the strain rate 100 s^{-1} to 1000 s^{-1} at the respective instant due to which the plug column will also be increased.

In Fig. 10b, at 100 µs, the impacted shape is formed like a spherical concave on the top layer of Al, and a convex surface appears on the backside of the Al layer due to the hemisphere nose of the projectile. At $t = 250$ µs, the middle part of the target plate appears at the backside of the target due to the shear failure of the Al sheet, and a small plug column form. The deformation of the CRALL increases as the contact area of the projectile increases during continuous ballistic penetration. Fiber tensile failure and shear failure happen in the CFRP composite layers. The delamination criterion occurs between the Al layer and the composite layer. In Fig. 9, the plug ejection failure mode is observed at the CRALL due to circumferential necking of shear. More shear deformation happens at a high strain rate. The perforated area remains constant after increasing the time $t > 400$ µs. The projectile's depth of penetration increases as the strain rate increases from 100 to 1000 s^{-1} at a time.

Similarly, Fig. 10c shows that at $t = 100$ µs, fiber tensile and matrix tensile failures are dominated by shear failure in the composite layer and tension failure occurs in the Al layers, resulting in a limited affected area and a considerable stress. At $t = 250$ µs and 400 µs, a sharp nose tip develops, indicating that the composite and both layers of Al have failed. As we increased the strain rate from 100 to 1000 s^{-1}, the rapid penetration process occurred at the same time. As seen in Fig. 9, the sharp-nosed projectile petalling failure mode is detected owing to redial tension in Al layers. However, petalling happens quickly when the rate of strain is increased. The depth of penetration of the bullet grows as the strain rate rises from 100 to 1000 s^{-1} at the corresponding instant, resulting in no plug column formation.

3.5 Energy absorption for the CRALL material

Energy absorption (internal energy) study of the CRALL/F, CRALL/H, and CRALL/S configurations is performed using the three different strain rates of 1, 100 and 1000 s^{-1} at a constant impactor velocity of 150 m/s, as shown in Fig. 11. It is observed that all the three cases (CRALL/F, CRALL/H, and CRALL/S) energy absorption are increasing with increases the strain rate from 1 to 1000 s^{-1}. The flat-nosed projectile has the highest energy absorption at 1000 s^{-1} strain rate when compared to other projectiles such as CRALL/H and CRALL/S at the same strain rate. It is due to the geometry of the projectile and higher strain rate effect. The CRALL/H material represents that the maximum and minimum energy absorptions are 11.8 J and 7.2 J for 1000 s^{-1} and 1 s^{-1}, respectively, at 0.4 ms. Similarly, the flat-nosed projectile impacted with CRALL material is also investigated, and the maximum and minimum energy absorptions are 60 J and 14 J for 1000 $s^{-1}$and 1 s^{-1}, respectively, at 0.8 ms. The sharp projectile impacted with CRALL material shows that the maximum and minimum energy absorptions are 10 J and 7 J for 1000 $s^{-1}$and 1 s^{-1} strain rates at 0.4 ms, respectively. Hence, it is concluded from these energy graphs that the energy absorption of the CRALL is proportional to the strain rate. This is the highest for the flat-nosed projectile, followed by the hemisphere and sharp projectiles.

4 Conclusion

The different projectile shapes and strain rate effects are numerically investigated for the CRALL under the HVI. From this numerical study, the major findings are as follows:

- The ballistic limit of the CRALL for all projectile impacts increases as the strain rate goes from 1 to 1000 s^{-1}. The residual velocity shows an inverse effect. This is due to the CRALL stiffening as a result of strain rates.
- For the flat-nosed projectile impact case, the CRALLs ballistic limit velocities are the highest at all strain rates, followed by hemisphere and sharp-nosed projectiles. This is because the flat-nosed projectile has the greatest initial contact area with the CRALL, followed by the hemisphere- and sharp-nosed projectiles.
- Raising the strain rate causes the yield strength and maximum strength to grow exponentially due to an increase in the Young modulus of elasticity.
- For the flat, hemisphere, and sharp-nosed projectiles, the CRALL failure patterns are shear, orthogonal cracks with a large hole, and orthogonal cracks with a small hole, respectively. This occurs as a result of their various interactions with the CRALL.
- At a 1s^{-1} strain rate, the yield strength of the CRALL is high for sharp-nosed projectiles and low for flat-nosed projectiles. At a high strain rate of 1000 s^{-1}, the yield strength of the target is high for hemisphere-nosed projectiles and low for flat-nosed projectiles. The maximum strength of the CRALL is the highest for flat-nosed projectiles at all strain rates.
- The flat-nosed projectile requires high velocity to perforate the target at both low and high strain rates and also showed the maximum energy absorption in comparison to other projectiles such as the CRALL/H and CRALL/S configurations.
- When the strain rate of the ballistic penetration process rises, the depth of penetration of the projectile increases. Increased strain rate had no significant influence on fiber tensile, matrix tensile, and delamination failures for the CRALL.
- The damage area is the largest for the CRALL/F configuration, followed by the CRALL/H and CRALL/S configuration.
- High tensile failure occurs at high strain rate for the CRALL/S, causing petalling in the CRALL for using the sharp projectiles.

Declarations

Conflict of interest The authors declare that they have no conflicts of interest.

References

1. Bahrami-Novin N, Shaban M, Mazaheri H (2022) Flexural response of fiber-metal laminate face-sheet/corrugated core sandwich beams. J Braz Soc Mech Sci Eng 44:1–14. https://doi.org/10.1007/s40430-022-03492-0
2. Vaiduriyam AR, Mailan Chinnapandi LB (2022) Experimental and numerical investigation of the vibro-acoustic behavior of fiber metal laminate. J Braz Soc Mech Sci Eng 44:1–31. https://doi.org/10.1007/s40430-022-03559-y
3. Ishak NM, Sivakumar D, Mansor MR (2018) The application of TRIZ on natural fiber metal laminate to reduce the weight of the car front hood. J Braz Soc Mech Sci Eng 40:1–12. https://doi.org/10.1007/s40430-018-1039-2
4. Song SH, Byun YS, Ku TW, Song WJ, Kim J, Kang BS (2010) Experimental and numerical investigation on impact performance of carbon reinforced aluminum laminates. J Mater Sci Technol 26:327–332. https://doi.org/10.1016/S1005-0302(10)60053-9
5. Naik NK, Yernamma P, Thoram NM, Gadipatri R, Kavala VR (2010) High strain rate tensile behavior of woven fabric E-glass/epoxy composite. Polym Test 29:14–22. https://doi.org/10.1016/j.polymertesting.2009.08.010
6. Rajkumar GR, Krishna M, Narasimhamurthy HN, Keshavamurthy YC, Nataraj JR (2014) Investigation of tensile and bending behavior of aluminum based hybrid fiber metal laminates. Procedia Mater Sci 5:60–68. https://doi.org/10.1016/j.mspro.2014.07.242
7. Naresh K, Shankar K, Velmurugan R, Gupta NK (2020) High strain rate studies for different laminate configurations of bidirectional glass/epoxy and carbon/epoxy composites using DIC. Structures 27:2451–2465. https://doi.org/10.1016/j.istruc.2020.05.022
8. Xia Y, Wang Y, Zhou Y, Jeelani S (2007) Effect of strain rate on tensile behavior of carbon fiber reinforced aluminum laminates. Mater Lett 61:213–215. https://doi.org/10.1016/j.matlet.2006.04.043
9. Wen HM (2000) Predicting the penetration and perforation of FRP laminates struck normally by projectiles with different nose shapes. Compos Struct 49:321–329. https://doi.org/10.1016/S0263-8223(00)00064-7
10. Kpenyigba KM, Jankowiak T, Rusinek A, Pesci R (2013) Influence of projectile shape on dynamic behavior of steel sheet subjected to impact and perforation. Thin-Walled Struct 65:93–104. https://doi.org/10.1016/j.tws.2013.01.003

11. Tirillò J, Ferrante L, Sarasini F, Lampani L, Barbero E, Sánchez-Sáez S, Valente T, Gaudenzi, (2017) High velocity impact behavior of hybrid basalt-carbon/epoxy composites. Compos Struct 168:305–312. https://doi.org/10.1016/j.compstruct.2017.02.039
12. Xu MM, Huang GY, Dong YX, Feng SS (2018) An experimental investigation into the high velocity penetration resistance of CFRP and CFRP/aluminium laminates. Compos Struct 188:450–460. https://doi.org/10.1016/j.compstruct.2018.01.020
13. Zhu Q, Zhang C, Curiel-Sosa JL, Bui TQ, Xu X (2019) Finite element simulation of damage in fiber metal laminates under high velocity impact by projectiles with different shapes. Compos Struct 214:73–82. https://doi.org/10.1016/j.compstruct.2019.02.009
14. Patel S, Soares CG (2018) Reliability assessment of glass epoxy composite plates due to low velocity impact. Compos Struct 200:659–668. https://doi.org/10.1016/j.compstruct.2018.05.131
15. Patel S, Ahmad S (2017) Probabilistic failure of graphite epoxy composite plates due to low velocity impact. J Mech Des 139:044501. https://doi.org/10.1115/1.4035678
16. Sierakowski, R. L. (1997). Strain rate effects in composites.
17. Groves SE, Sanchez RJ, Lyon RE, Brown AE (1993) High strain rate effects for composite materials. ASTM Spec Tech Publ 1206:162–162
18. Yen CF (2012) A ballistic material model for continuous-fiber reinforced composites. Int J Impact Eng 46:11–22. https://doi.org/10.1016/j.ijimpeng.2011.12.007
19. Al-Hassani, S. T. S., &Kaddour, A. S. (1998). Strain rate effects on GRP, KRP and CFRP composite laminates. In: Key engineering materials, vol 141, pp 427–452. Trans Tech Publications Ltd.https://doi.org/10.4028/www.scientific.net/kem.141-143.427.
20. Hsiao H, Daniel IM (1998) Strain rate behavior of composite materials. Compos B Eng 29(5):521–533. https://doi.org/10.1016/S1359-8368(98)00008-0
21. Ma D, Manes A, Amico SC, Giglio M (2019) Ballistic strain-rate-dependent material modelling of glass-fibre woven composite based on the prediction of a meso-heterogeneous approach. Compos Struct 216:187–200. https://doi.org/10.1016/j.compstruct.2019.02.102
22. Ma D, Wang Z, Giglio M, Amico SC, Manes A (2022) Influence of strain-rate related parameters on the simulation of ballistic impact in woven composites. Compos Struct 300:116142. https://doi.org/10.1016/j.compstruct.2022.116142
23. Xiao L, Xu X, Wang H (2022) A comparative study of finite element analysis of single-particle impact on mild steel with and without strain rate considered. Int J Impact Eng 159:104029. https://doi.org/10.1016/j.ijimpeng.2021.104029
24. Smahat A, Mankour A, Slimane S, Roubache R, Bendine K, Guelailia A (2020) Numerical investigation of debris impact on spacecraft structure at hyper-high velocity. J Braz Soc Mech Sci Eng 42(3):1–13. https://doi.org/10.1007/s40430-020-2196-7
25. Karim MR, Fatt MS (2006) Rate-dependent constitutive equations for carbon fiber-reinforced epoxy. Polym Compos 27:513–528. https://doi.org/10.1002/pc.20221
26. Patel S, Patel M (2022) The efficient design of hybrid and metallic sandwich structures under air blast loading. J Sandw Struct Mater 24:1706–1725. https://doi.org/10.1177/10996362211065748
27. Patel M, Patel S (2022) Novel design of honeycomb hybrid sandwich structures under air-blast. J Sandw Struct Mater 24(8):2105–2123. https://doi.org/10.1177/10996362221127967
28. Daniel IM, LaBedza RH (1983) Method for compression testing of composite materials at high. In: Compression testing of homogeneous materials and composites: a symposium, No 808, p 121. ASTM International.
29. He ZF, Jia N, Wang HW, Liu Y, Li DY, Shen YF (2020) The effect of strain rate on mechanical properties and microstructure of a metastable FeMnCoCr high entropy alloy. Mater Sci Eng A 776:138982. https://doi.org/10.1016/j.msea.2020.138982
30. Hund J, Granum HM, Olufsen SN, Holmström PH, Johnsen J, Clausen AH (2022) Impact of stress triaxiality, strain rate, and temperature on the mechanical response and morphology of PVDF. Polym Test 114:107717. https://doi.org/10.1016/j.polymertesting.2022.107717
31. Kun Q, Li-Ming Y, Shi-Sheng H (2009) Mechanism of strain rate effect based on dislocation theory. Chin Phys Lett 26(3):036103. https://doi.org/10.1088/0256-307X/26/3/036103
32. Seo JM, Kim HT, Kim YJ, Yamada H, Kumagai T, Tokunaga H, Miura N (2022) Effect of strain rate and stress triaxiality on fracture strain of 304 stainless steels for canister impact simulation. Nucl Eng Technol. https://doi.org/10.1016/j.net.2022.02.002
33. Wang W, Ma Y, Yang M, Jiang P, Yuan F, Wu X (2017) Strain rate effect on tensile behavior for a high specific strength steel: from quasi-static to intermediate strain rates. Metals 8(1):11. https://doi.org/10.3390/met8010011